EES Catalysis

Check for updates

Variable-valence element doping mediated photogenerated electron trapping for selective oxidation reactions†

Xia Zhong,‡ Yan Zhao,‡ Lei Li, [iD] Xin He, Hui Wang,* Xiaodong Zhang [iD] * and Yi Xie [iD] *

Photocatalytic selective oxidation provides a green and mild way of producing high-value added chemicals, whose conversion and selectivity are limited by complex oxidation pathways mediated by various reactive radical species. Thus, using photogenerated holes as an oxidant to directly drive these oxidation reactions could overcome the above problems, whereas the simultaneously formed electrons would cause the quenching of holes or the formation of other unfavorable reactive oxygen species that would affect the reaction efficiency. Herein, a variable-valence element doping method was proposed to realize hole-mediated photocatalytic selective oxidation. By taking Cu-doped Bi_2WO_6 as a typical prototype, we show that the doped Cu element with monovalent and divalent character can effectively trap photogenerated electrons, thereby boosting hole accumulation for selective oxidation reactions. As expected, Cu-doped Bi_2WO_6 exhibited excellent catalytic performances in oxidative coupling of benzylamines. This study provides a perspective on optimizing selective oxidation by hole regulation.

Broader context

Photocatalytic selective oxidation is considered a green route for the synthesis of high value-added organic chemicals. However, the complex reaction pathways caused by a variety of free radicals limit the conversion and selectivity of photocatalysis. Using holes as a single oxidant is a promising strategy for photocatalytic selective oxidation. Herein, variable-valence element Cu is introduced into the semiconductor-based photocatalyst Bi_2WO_6 as electron-trapping sites to regulate the hole behavior. Both experimental and theoretical investigations show that the impurity level dominated by Cu states could effectively capture photogenerated electrons, thus allowing more holes to participate in selective oxidation reactions. In addition, Cu-doping-induced reconstruction of the electronic structure of Bi_2WO_6 not only promotes the dissociation of excitons in the confined layered structure to free carriers, but also optimizes the transport properties of the sample. Owing to the above advantages, Cu-doped Bi_2WO_6 shows excellent conversion and selectivity in photocatalytic oxidative coupling of amines.

Introduction

Selective oxidation is one of the largest industrial processes in producing modern chemicals, and plenty of important intermediates such as imines, epoxides and aldehydes are synthesized by using suitable oxidants.[1–3] In general, these organic reactions are usually carried out under harsh conditions such as high temperature and pressure, accompanied by high energy consumption and environmental pollution. Photocatalytic selective oxidation triggered by semiconductor-based photocatalysts

Hefei National Research Center for Physical Sciences at the Microscale, University of Science and Technology of China, Hefei, Anhui 230026, China. E-mail: wanghuig@ustc.edu.cn, zhxid@ustc.edu.cn, yxie@ustc.edu.cn

† Electronic supplementary information (ESI) available. See DOI: https://doi.org/10.1039/d4ey00024b

‡ These authors contributed equally to this work.

provides a green and mild way of preparing high value-added organic compounds.[4] Although some progress has been made, photocatalytic oxidation reactions still face the problem of low selectivity, due to the continuous and complex character of reaction processes.[5,6] For example, the parallel oxidation pathways dominated by different photoinduced reactive radical species would result in a wide product distribution.[7] In that case, controlling the generation of certain oxidants is considered to be the key scientific problem in photocatalytic selective oxidation reactions. As is known, reactive oxygen species (ROS) and photogenerated holes are the dominant oxidants for photocatalytic aerobic oxidation reactions.[8] Generally, ROS including superoxide, singlet oxygen, and hydroxyl radicals with various lifetimes and oxidizability may trigger uncontrolled oxidation processes or even destruction of substrates and products.[9,10] In contrast, directly using holes as a single

oxidant to initiate photocatalytic organic oxidation would be a promising pathway in avoiding overoxidation reactions.

As for the semiconductor-based photocatalysts, electrons and holes are photogenerated simultaneously, and thus sacrificial agents to quench electrons are widely used to boost the accumulation of holes during the reaction. However, these sacrificial agents, such as potassium persulfate and 2,3-dichloro-5,6-dicyano-1,4-benzoquinone, are difficult to separate from the reaction system, resulting in the pollution of the products. Alternatively, constructing an electron trap state in the semiconductor-based photocatalysts would be a practical way of offering selective hole accumulation and avoiding the use of external agents.[11] Besides, in order to preserve the trapped photogenerated electrons, the trap state should store electrons at the same time. Bearing this in mind, we pay our attention to element doping, which has attracted extensive attention due to its advantages in regulating the electronic band structure, promoting charge separation, expanding light absorption, and so on.[12–14] Meanwhile, the introduction of variable-valence elements, such as Cu with monovalent and divalent character, could not only generate an impurity state, but also offer a redox pair based on Cu(II)/Cu(I), as schematically illustrated in Scheme 1.[15–18]

Herein, a typical layered semiconductor, bismuth tungstate (Bi_2WO_6), with ideal visible light absorption was selected as a model, and we interrogated the feasibility of variable-valence Cu doping in regulating the involved photogenerated hole behaviors. Density functional theory (DFT) calculations show that Cu doping forms a deep impurity level and reconstructs the electronic structure of Bi_2WO_6 (Fig. 1a and b). Compared with shallow states, these deep states could effectively trap photogenerated electrons and prolong the lifetime of holes, which are favorable to hole-mediated photocatalytic selective oxidation.[19,20] In addition, the homogeneities of the valence and conduction band-edge states are broken in $Cu–Bi_2WO_6$, which could facilitate the dissociation of excitons in the confined layered structure into free carriers.[21] Band-edge charge density isosurfaces show that the charge of the conduction band in $Cu–Bi_2WO_6$ is mainly localized at Cu sites, while that of the pristine Bi_2WO_6 is mainly distributed in the $[WO_4]^{2-}$ layers (Fig. 1c–f). Electron trapping at Cu sites could effectively restrain the recombination of photogenerated electrons and

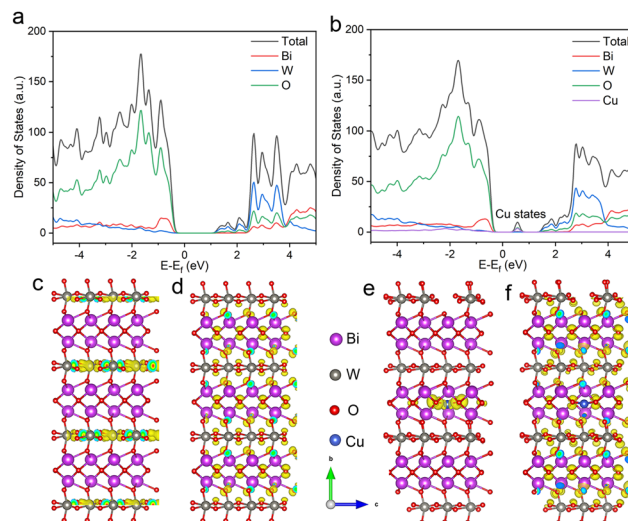**Fig. 1** Calculated density of states of (a) Bi_2WO_6 and (b) $Cu–Bi_2WO_6$. Band-edge charge density isosurfaces of the Bi_2WO_6 (c) conduction and (d) valence bands; band-edge charge density isosurfaces of the $Cu–Bi_2WO_6$ (e) conduction and (f) valence bands.

holes, and promote the encounter of the holes and substrates. Therefore, $Cu–Bi_2WO_6$ is expected to exhibit excellent performance in photocatalytic selective oxidation reactions.

Results and discussion

In this work, Cu-doped Bi_2WO_6 ($Cu–Bi_2WO_6$) and pristine Bi_2WO_6 were synthesized through a hydrothermal method. The powder X-ray diffraction patterns (XRD) of the as prepared samples shown in Fig. 2a suggested similar structures of them, which could be well indexed to an orthorhombic phase of Bi_2WO_6 (JCPDS No. 73-2020). As shown in Fig. S1 (ESI†), the transmission electron microscopy (TEM) images of $Cu–Bi_2WO_6$ and pristine Bi_2WO_6 indicated their 2D sheet-like morphologies. The high-resolution TEM (HRTEM) image of the $Cu–Bi_2WO_6$ nanosheets in Fig. 2b displays distinct mutually perpendicular lattice fringes with an interplanar spacing of 0.27 nm, and the fast Fourier transition (FFT) pattern of the top facet obviously determines the two crystal plane orientations, and the angle labelled is $90°$ which is consistent with the theoretical value between the
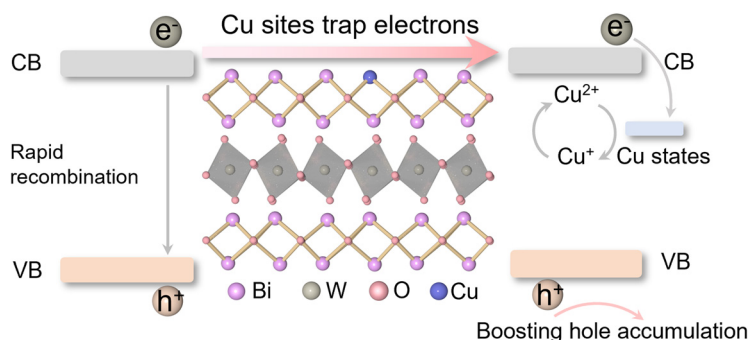
Scheme 1 A scheme of variable-valence Cu doping in Bi_2WO_6 for capturing photogenerated electrons and boosting hole accumulation.
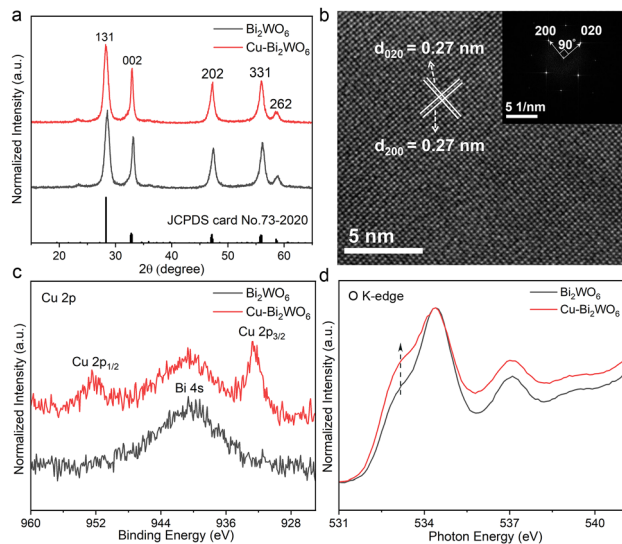
Fig. 2 (a) XRD patterns of Bi_2WO_6 and $Cu-Bi_2WO_6$. (b) HRTEM image of $Cu-Bi_2WO_6$ (Inset: The corresponding FFT pattern). (c) High-resolution Cu 2p XPS spectra and (d) O K-edge XANES spectra of Bi_2WO_6 and $Cu-Bi_2WO_6$.

(020) and (200) planes.[22] Bi_2WO_6 exhibits similar lattice fringes (Fig. S2, ESI†). The energy-dispersive X-ray spectroscopy (EDS) (Fig. S3, ESI†) elemental mapping and electron probe micro-analysis (EPMA) (Fig. S4, ESI†) confirm the existence of homo-geneously distributed Cu in elemental doped Bi_2WO_6. The content of doped Cu is estimated to be about 0.2 wt% in $Cu-Bi_2WO_6$ by inductively coupled plasma atomic emission spectroscopy (ICP-AES). Furthermore, X-ray photoelectron spectroscopy (XPS) was used to analyse the chemical composi-tions and surface chemical states of the related elements. The peaks observed at around 952.5 eV and 932.7 eV can be attributed to the Cu $2p_{1/2}$ and Cu $2p_{3/2}$ levels, respectively, providing direct evidence for the existence of surface copper (Fig. 2c). Note that the peak around 940 eV is indexed to Bi 4s. Meanwhile, both Bi 4f spectra and W 4f spectra (Fig. S5, ESI†) are almost comparable for the two samples, indicating that their chemical states are hardly affected by the copper. As shown in Fig. S6 (ESI†), the peak at 720 cm^{-1} of the Raman spectra was interpreted as an antisymmetric bridging mode, associated with the tungstate chains. The characteristic bands near 795 cm^{-1} and 830 cm^{-1} could be assigned to the asym-metric and symmetric vibrations of O–W–O, respectively.[23] For $Cu-Bi_2WO_6$, the symmetric stretching vibration of the O–W–O bond is weakened, indicating that copper doping would effec-tively modify the O–W–O vibration scenarios. X-ray absorption near-edge structure (XANES), a strong technique to study the electronic structure of materials, was carried out to reveal the effect of Cu doping on Bi_2WO_6. The O K-edge XANES spectra in Fig. 2d reveal a main peak located at the X-ray energy of 534.4 eV with a shoulder peak at 533.2 eV for both samples. Compared with Bi_2WO_6, the intensity of the shoulder peak in $Cu-Bi_2WO_6$ showed a sharp increase, indicating the rehybridi-zation of O 2p and Bi 6p due to local structural distortion

associated with Cu doping.[24] And the electron occupied state of the oxygen atom in $Cu-Bi_2WO_6$ decreased in comparison to the pristine sample, which is possibly related to electron trapping at the Cu sites.[25] Besides, both samples exhibit similar Brun-ner–Emmett–Teller (BET) surface area (Fig. S7, ESI†). According to the above characterization and analysis, we could confirm that Cu-doped Bi_2WO_6 with local structural distortion was successfully prepared.

Elemental doping can greatly influence the optical proper-ties and band structures of photocatalysts. As shown in Fig. 3a, there is an additional absorption tail in the UV-vis spectra of $Cu-Bi_2WO_6$ as compared to the undoped sample, which might be related to plenty of defects formed by Cu doping.[26] Mean-while, the valence band maximum (VBM) shifted toward lower energy in $Cu-Bi_2WO_6$, closer to the Fermi level, indicating that the hole concentration increased after Cu doping (Fig. S8, ESI†).[27] Such broad band-offset in the VBM suggests the inter-play between the different types of valence bands, which would contribute to the transport properties of the hole.[28] In addition to the band structures and transport properties, Cu doping also has a dramatic impact on photogenerated species. As seen in the low temperature fluorescence spectra (PL), compared with pristine Bi_2WO_6, the emission peak of the exciton ($\sim$567 nm) in $Cu-Bi_2WO_6$ is negligible, implying that excitons dissociate into free electrons and holes (Fig. 3b).[29] Moreover, the PL spectra of $Cu-Bi_2WO_6$ reveal a remarkable lower intensity as compared to the pristine sample, indicating its suppressed recombination of photoexcited electrons and holes. Time-resolved phosphores-cence (PH) spectra (Fig. S9, ESI†) of the two samples were measured to investigate the dynamics of the charge carrier, where $Cu-Bi_2WO_6$ shows a shorter PH life compared with Bi_2WO_6, indicating its fast electron transfer. Weaker PL emission intensity and shorter PH lifetime manifest that Cu doping might effectively promote the photogenerated electron extraction to the Cu sites.[30]
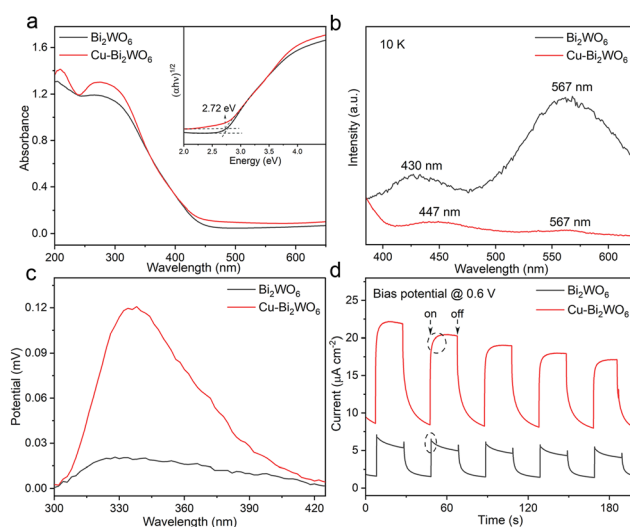
Fig. 3 (a) UV-vis absorption spectra (Inset: The corresponding Tauc plots), (b) low-temperature (10 K) steady-state photoluminescence emis-sion spectra, (c) SPV spectra and (d) the periodic on/off photocurrent responses of Bi_2WO_6 and $Cu-Bi_2WO_6$ samples.

The surface photovoltage (SPV) (Fig. 3c) and the transient photocurrent response (Fig. 3d) were also used to investigate the carrier separation efficiency. The drastically improved intensity of the SPV signal and the transient photocurrent response had demonstrated improved photogenerated carrier concentration after photoexcitation in Cu–Bi$_2$WO$_6$. In detail, Bi$_2$WO$_6$ shows spikes in the photocurrent, which is generally interpreted as rapid recombination of carriers in Bi$_2$WO$_6$. For Cu–Bi$_2$WO$_6$, as light cuts on, the photocurrent did not rise directly to the highest value, but had a slow rising process. This phenomenon can be understood as that part of the charge carriers are gradually captured by the Cu sites and cannot transmit charge, inhibiting the increase in photocurrent. The photocurrent shows a trailing curve as the light cuts off, which is because of the release of previously trapped charge in Cu sites.[31] Electrochemical impedance spectroscopy (EIS) was carried out to detect charge transfer characteristics of the samples (Fig. S10, ESI†), where the Cu–Bi$_2$WO$_6$ possesses smaller charge-transfer resistance (R_{ct}) than that of Bi$_2$WO$_6$, revealing the enhanced charge-transfer process and conductivity. Thus, the results clearly demonstrate that electron capture at Cu sites improves the carrier separation efficiency and optimizes the transport properties of the sample.

In order to reveal the electron capture at Cu sites of Cu–Bi$_2$WO$_6$, *in situ* XPS experiments were performed to study the chemical state of Cu–Bi$_2$WO$_6$ in photocatalysis. Fig. 4a shows XPS spectra of Cu 2p in the dark and under irradiation conditions. The peak observed at around 933.7 eV can be attributed to Cu^{2+}, and the peak observed at around 932.2 eV is assigned to Cu^0/Cu$^+$.[32] It is interesting that the concentration of Cu^0/Cu$^+$ in Cu–Bi$_2$WO$_6$ increased from 73.3% to 83.7% after light irradiation, which could be understood as the photogenerated electron accumulation on the Cu^{2+} species, beneficial for

the hole generation. Besides, the Bi 4f and W 4f *in situ* XPS spectra of Cu–Bi$_2$WO$_6$ exhibit tailing in the low binding energy direction under light irradiation (Fig. S11, ESI†), indicating the appearance of lower chemical states of Bi and W species. *In situ* ESR spectra under different conditions were also used to unravel the chemical state of the copper species, where Cu–Bi$_2$WO$_6$ exhibited a strong signal of Cu^{2+} in dark conditions, and hyperfine structure could be observed through the ESR spectra since $I = 3/2$ of Cu^{2+} (Fig. 4b).[33] Upon illumination, the intensity of Cu^{2+} decreased, indicating that Cu^{2+} could accept electrons to form ESR-silent Cu$^+$, confirming the presence of electron capture in the Cu sites. *In situ* ESR spectra of Bi$_2$WO$_6$ (Fig. S12, ESI†) turned out to possess a typical weak ESR signal centered at $g = 2.003$ owing to electron trapped oxygen vacancies. Furthermore, XANES measurements under dark and light conditions were carried out to study the influence of carrier trapping by Cu doping. As shown in Fig. 4c, the shoulder peak of Cu–Bi$_2$WO$_6$ changed insignificantly under light conditions compared with the pristine Bi$_2$WO$_6$, indicating that the electron occupied state of the O element had no evident changes in Cu–Bi$_2$WO$_6$ after illumination. Combined with XPS analysis, it can be inferred that owing to the strong electron trapping ability of Cu sites, photogenerated electrons are more easily captured by Cu sites rather than O atoms in Cu–Bi$_2$WO$_6$, which is conducive to improving the tolerance for illumination and stability of the sample. The above *in situ* tests have proved that Cu doping can trap photogenerated electrons and extend the lifetime of the holes, which can be demonstrated by the oxygen activation behavior. Generally, the hydroxyl radical ($^\bullet$OH) is generated by the oxidation of adsorbed water, whose generation was dependent on the hole concentration of the system. As shown in Fig. S13 (ESI†), Cu–Bi$_2$WO$_6$ has a strong ESR signal, while Bi$_2$WO$_6$ generates almost no $^\bullet$OH, indicating that Cu–Bi$_2$WO$_6$ has a strong ability to generate holes. Due to the electron capture at the Cu sites, Cu–Bi$_2$WO$_6$ has a weak ability to activate oxygen into a superoxide anion radical ($^\bullet$O$_2^-$) (Fig. S14a and b, ESI†). Complementary evolutions of $^\bullet$OH and $^\bullet$O$_2^-$ in Cu–Bi$_2$WO$_6$ further confirmed the positive role of Cu doping on the electron capture and hole accumulation. According to all the analysis above and Mott–Schottky plots (Fig. S15, ESI†), we drew the band structure diagram (Fig. 4d), and proposed the catalytic mechanism of Cu–Bi$_2$WO$_6$. In detail, electrons and holes are generated by photoexcitation in Cu–Bi$_2$WO$_6$, and electrons in the conduction band are captured by the Cu states, resulting in the reduction of Cu(II) to Cu(I), which could be reversed *via* electron-mediated molecular oxygen activation. According to the DFT calculation (Fig. 1b), the Cu-impurity state in Cu–Bi$_2$WO$_6$ is far lying above the conduction band, that is, electrons trapped by these states have insufficient reduction potential to trigger O$_2$ to $^\bullet$O$_2^-$ conversion, which could be confirmed by weaker generation of $^\bullet$O$_2^-$ in Cu–Bi$_2$WO$_6$. The selective removal of photogenerated electrons suppresses hole consumption and hence facilitates the accumulation of holes in the system, which directly leads to the utilization efficiency of photogenerated holes being significantly elevated for selective oxidation reactions.
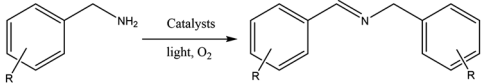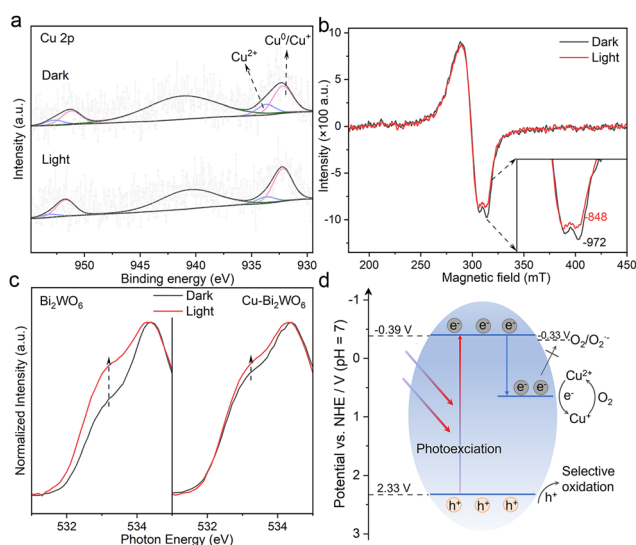

Fig. 4 (a) *In situ* high-resolution Cu 2p XPS spectra and (b) *in situ* ESR spectra of Cu–Bi$_2$WO$_6$ under dark and illumination conditions. (c) *In situ* O K-edge XANES spectra of Bi$_2$WO$_6$ and Cu–Bi$_2$WO$_6$ under dark and illumination conditions. (d) Band structure diagram of Cu–Bi$_2$WO$_6$.

Table 1 Selective oxidative coupling of amines[a]

Entry	R	Time (h)	Bi$_2$WO$_6$		Cu-Bi$_2$WO$_6$	
			Conv.[b] (%)	Sel.[c] (%)	Conv.[b] (%)	Sel.[c] (%)
1	H	16	28	84	99	99
2[d]	H	16	Trace	Trace	Trace	Trace
3[e]	H	16	12	12	48	48
4	m-F	16	27	73	78	97
5	p-Cl	12	19	99	84	99
6	m-Cl	16	27	99	76	99
7	p-Br	16	28	65	88	93
8	m-Me	16	34	95	95	97
9	p-Me	16	30	70	91	91
10	p-OMe	16	43	91	77	93

[a] Reaction conditions: substrate (0.2 mmol), catalyst (10 mg), trifluorotoluene (2 mL), O$_2$ (1 atm), 298 K, xenon lamp (CEL-PF300-T10, Beijing China Education Au-light Technology Co. Ltd) with a cutoff filter ($\lambda \geq$ 420 nm). [b] Determined by NMR analyses, using 1,1,2,2-tetrachloroethane as the internal standard, mol%. [c] Selectivity = yield$_{imine}$ × 2/conversion$_{amine}$, mol%. [d] Argon atmosphere. [e] Additional 300 μL of methanol.

In view of its boosting hole accumulation and optimizing transport properties, Cu–Bi$_2$WO$_6$ is expected to be an ideal photocatalyst for selective oxidation, such as oxidation of amines to the corresponding imines. Imines and their derivatives are important multifunctional organic intermediates, which are widely used in biology, pharmaceuticals and fine chemical areas.[34] Here, selective oxidative coupling of benzylamines was carried out to evaluate the photocatalytic performance of Cu–Bi$_2$WO$_6$. As shown in Table 1, Cu–Bi$_2$WO$_6$ exhibited better oxidizability and selectivity than that of pristine Bi$_2$WO$_6$, where oxygen plays an important role in the reaction process (entry 2). Since O$_2$ to $^\bullet$O$_2^-$ conversion is inhibited in Cu–Bi$_2$WO$_6$ (Fig. S14a and b, ESI†), the oxygen in this system would mainly oxidize low-valence Cu(I) to Cu(II) to realize the cycle between the redox pair of Cu, thereby promoting the continuous formation of holes for oxidative coupling of benzylamine. In detail, entry 1 indicates that the conversion rate of Cu-Bi$_2$WO$_6$ (99%) is three times that of Bi$_2$WO$_6$ (28%). The introduction of methanol as the sacrificial agent for holes in the reaction could suppress the oxidative coupling of benzylamine, indicating the critical role of holes for the selective oxidation (entry 3). Based on the band structure of Cu–Bi$_2$WO$_6$ (Fig. 4d), the valence band maximum of Cu–Bi$_2$WO$_6$ is 2.33 V, which is located at a more positive position than the oxidation potential of benzylamine (0.76 V vs. NHE).[35] Thus, the hole in the valence band contributed to oxidation of benzylamine to N-centered free-radical C$_6$H$_5$CH$_2$NH$_2^{\bullet+}$ in the coupling process (Fig. S16 and S17, ESI†). Besides, we further select a series of benzylamine derivatives to explore the scope of this oxidative coupling of benzylamines reaction. It could be seen that Cu–Bi$_2$WO$_6$ exhibits better catalytic performance than that of Bi$_2$WO$_6$, whether with electron-withdrawing (entries 4–7) or electron-donating (entries 8–10) groups. The excellent catalytic

performance of Cu–Bi$_2$WO$_6$ has contributions from the comprehensive regulation of hole behavior and transport properties by copper doping, which renders Cu–Bi$_2$WO$_6$ to be a promising catalyst in selective oxidation reactions.

Conclusions

In summary, a variable-valence element method was proposed to regulate the behavior of photogenerated holes in semiconductor-based photocatalysts for highly efficient selective oxidation reactions. By taking Cu-doped Bi$_2$WO$_6$ as a proof-of-concept model, theoretical and experimental results have proved that Cu element doping would cause energetic disorder to promote exciton dissociation to carriers in the Bi$_2$WO$_6$ system. What is more, the deep impurity level formed by Cu doping can effectively trap photogenerated electrons, obviously improving the concentration and mobility of hole. Besides, the electron-trapping induced reduction of Cu(II) to Cu(I) contributes to improving the transport properties of Bi$_2$WO$_6$. Owing to these advantages, Cu–Bi$_2$WO$_6$ exhibits excellent photocatalytic performance in selective oxidation of amines to imines. This study provides a feasible method for hole-behavior regulation in semiconductor-based photocatalysts for achieving excellent performance in selective oxidation reactions.

Experimental

Preparation of samples

Cu-Bi$_2$WO$_6$ was synthesized by a simple hydrothermal method. In detail, 2 mmol bismuth nitrate pentahydrate and 0.15 mmol copper(II) nitrate trihydrate were added to 20 mL acetic acid solution, and 1 mmol sodium tungsten oxide dihydrate was added to 10 mL water, denoted as solutions A and B, respectively. After the solution is fully dissolved, solution B was added to solution A drop by drop. After stirring for 30 min, the mixture was transferred to a 50 mL Teflon-lined autoclave and heated at 180 °C for 12 hours. After natural cooling to room temperature, the precipitation was collected and washed several times with ethanol and distilled water, and then dried under vacuum overnight. For Bi$_2$WO$_6$, except for the fact that copper(II) nitrate trihydrate is not added during the synthetic process, the other synthetic steps are consistent with the above method.

Material characterizations

The transmission electron microscopy (TEM), high-resolution transmission electron microscopy (HRTEM) and energy dispersive spectrometer (EDS) measurements were performed on a Talos F200X field emission electron microscope with an acceleration voltage of 200 kV. The NMR experiments were conducted with a 400-MHz Bruker AVANCE AV III NMR spectrometer. The X-ray diffraction (XRD) spectra were acquired by a Philips X'Pert Pro Super diffractometer with Cu-Kα radiation (λ = 1.54178 Å). The X-ray photoelectron spectra (XPS) were obtained on an ESCALAB MKII based on C 1s (284.6 eV) and Mg Kα as the excitation source. The ESR trapping experiments were

Paper

EES Catalysis

performed on a Jeol JES-FA200 X-band ESR spectrometer. The electrochemical measurements were delivered by an electrochemical workstation (CHI760E, Shanghai Chenhua Limited, China). The X-ray absorption near-edge structure (XANES) spectra were tested at the Beamlines MCD-A and MCD-B (Soochow Beamline for Energy Materials) at the National Synchrotron Radiation Laboratory (NSRL). UV-vis spectra were acquired on a PerkinElmer Lambda 950 UV-vis-NIR spectrophotometer. The steady-state fluorescence and the time-resolved phosphorescence spectra were obtained on a FLUOROLOG-3-TAU fluorescence spectrometer.

Electron spin resonance (ESR)-trapping measurements

ESR-trapping tests in water can detect $^{\bullet}OH$ by utilizing the tapping reagent DMPO (5,5-dimethyl-1-pyrroline N-oxide). 500 μL of distilled water, 50 μL of DMPO (10 mM) solution and 50 μL of aqueous suspension of the samples (10 mg mL^{-1}) were mixed. After irradiation for 1 min, the mixture was characterized by using a JEOL JES-FA200 electron spin resonance spectrometer (298 K, 9.097 GHz). For the test of amine free-radicals, using DMPO as the radical trapping reagent, 500 μL of acetonitrile, 50 μL of DMPO (10 mM) solution, 20 μL benzylamine and 50 μL of acetonitrile suspension of the sample (10 mg mL^{-1}) were mixed. The signals were collected under dark and light irradiation.

Calculation method

The present first principle DFT calculations are performed by the Vienna Ab initio Simulation Package (VASP)[36] with the projector augmented wave (PAW) method.[37] The self-consistent calculations apply a convergence energy threshold of 10^{-5} eV. The exchange-functional is treated using the generalized gradient approximation (GGA) of the Perdew–Burke–Ernzerhof (PBE)[38] functional. The Brillouin zone integration was performed using $3 \times 2 \times 3$ k-point sampling for both structure optimization and electron self-consistent calculation, respectively. The energy cutoff for the plane wave basis expansion was set to 450 eV and the force on each atom of less than 0.02 eV Å^{-1} was set for the convergence criterion of geometry relaxation. A $2 \times 1 \times 2$ supercell of Bi_2WO_6 was adopted for further calculations, while one Bi atom was replaced by a Cu atom in the Cu doping model.

Conflicts of interest

There are no conflicts to declare.

Acknowledgements

Notes and references

1 L. Xiong and J. Tang, *Adv. Energy Mater.*, 2021, **11**, 2003216.
2 X. Liu, R. Qi, S. Li, W. Liu, Y. Yu, J. Wang, S. Wu, K. Ding and Y. Yu, *J. Am. Chem. Soc.*, 2022, **144**, 23396–23404.
3 H. Wang, C. Cao, D. Li, Y. Ge, R. Chen, R. Song, W. Gao, X. Wang, X. Deng, H. Zhang, B. Ye, Z. Li and C. Li, *J. Am. Chem. Soc.*, 2023, **145**, 16852–16861.
4 G. Ciamician, *Science*, 1912, **36**, 385–394.
5 X. Xiao, Z. Ruan, Q. Li, L. Zhang, H. Meng, Q. Zhang, H. Bao, B. Jiang, J. Zhou, C. Guo, X. Wang and H. Fu, *Adv. Mater.*, 2022, **34**, 2200612.
6 G. Palmisano, V. Augugliaro, M. Pagliaro and L. Palmisano, *Chem. Commun.*, 2007, 3425–3437.
7 J. Tripathy, K. Lee and P. Schmuki, *Angew. Chem., Int. Ed.*, 2014, **53**, 12605–12608.
8 Y. Nosaka and A. Y. Nosaka, *Chem. Rev.*, 2017, **117**, 11302–11336.
9 W. Liu, Y. Wang, H. Huang, J. Wang, G. He, J. Feng, T. Yu, Z. Li and Z. Zou, *J. Am. Chem. Soc.*, 2023, **145**, 7181–7189.
10 Z. Tian, C. Han, Y. Zhao, W. Dai, X. Lian, Y. Wang, Y. Zheng, Y. Shi, X. Pan, Z. Huang, H. Li and W. Chen, *Nat. Commun.*, 2021, **12**, 2039.
11 A. Yamakata, J. J. M. Vequizo and H. Matsunaga, *J. Phys. Chem. C*, 2015, **119**, 24538–24545.
12 W. Shao, H. Wang and X. Zhang, *Dalton Trans.*, 2018, **47**, 12642–12646.
13 C. Liu, D. Hao, J. Ye, S. Ye, F. Zhou, H. Xie, G. Qin, J. Xu, J. Liu, S. Li and C. Sun, *Adv. Energy Mater.*, 2023, **13**, 2204126.
14 Y. Shi, Z. Yang, L. Shi, H. Li, X. Liu, X. Zhang, J. Cheng, C. Liang, S. Cao, F. Guo, X. Liu, Z. Ai and L. Zhang, *Environ. Sci. Technol.*, 2022, **56**, 14478–14486.
15 X. Chen, S. Xiao, H. Wang, W. Wang, Y. Cai, G. Li, M. Qiao, J. Zhu, H. Li, D. Zhang and Y. Lu, *Angew. Chem., Int. Ed.*, 2020, **59**, 17182–17186.
16 W. Xie, Y. Liu, X. Zhang, H. Yan, X.-H. Liu, X. Zhang, Q. Zhao and H. Huang, *Angew. Chem., Int. Ed.*, 2024, **63**, e202314384.
17 J. Yang, W. Liu, M. Xu, X. Liu, H. Qi, L. Zhang, X. Yang, S. Niu, D. Zhou, Y. Liu, Y. Su, J.-F. Li, Z.-Q. Tian, W. Zhou, A. Wang and T. Zhang, *J. Am. Chem. Soc.*, 2021, **143**, 14530–14539.
18 M. Zheng, P. Wang, X. Zhi, K. Yang, Y. Jiao, J. Duan, Y. Zheng and S.-Z. Qiao, *J. Am. Chem. Soc.*, 2022, **144**, 14936–14944.

19 J. J. M. Vequizo, H. Matsunaga, T. Ishiku, S. Kamimura, T. Ohno and A. Yamakata, *ACS Catal.*, 2017, **7**, 2644–2651.

20 E. Pastor, M. Sachs, S. Selim, J. R. Durrant, A. A. Bakulin and A. Walsh, *Nat. Rev. Mater.*, 2022, **7**, 503–521.

21 Y. Shi, G. Zhan, H. Li, X. Wang, X. Liu, L. Shi, K. Wei, C. Ling, Z. Li, H. Wang, C. Mao, X. Liu and L. Zhang, *Adv. Mater.*, 2021, **33**, 2100143.

22 Y. Zhou, Y. Zhang, M. Lin, J. Long, Z. Zhang, H. Lin, J. C.-S. Wu and X. Wang, *Nat. Commun.*, 2015, **6**, 8340.

23 H. Huang, C. Zhou, X. Jiao, H. Yuan, J. Zhao, C. He, J. Hofkens, M. B. J. Roeffaers, J. Long and J. A. Steele, *ACS Catal.*, 2020, **10**, 1439–1443.

24 C.-H. Chen, B.-J. Hwang, C.-Y. Chen, S.-K. Hu, J.-M. Chen, H.-S. Sheu and J.-F. Lee, *J. Power Sources*, 2007, **174**, 938–943.

25 F. Frati, M. O. J. Y. Hunault and F. M. F. de Groot, *Chem. Rev.*, 2020, **120**, 4056–4110.

26 H. Li, J. Li, Z. Ai, F. Jia and L. Zhang, *Angew. Chem., Int. Ed.*, 2018, **57**, 122–138.

27 H. Kang, J. Li, Y. Liu, E. Guo, Z. Chen, D. Liu, G. Fan, Y. Zhang, X. Jiang and T. Wang, *J. Mater. Chem. C*, 2018, **6**, 8479–8487.

28 J. Androulakis, I. Todorov, D.-Y. Chung, S. Ballikaya, G. Wang, C. Uher and M. Kanatzidis, *Phys. Rev. B: Condens. Matter Mater. Phys.*, 2010, **82**, 115209.

29 H. Wang, D. Yong, S. Chen, S. Jiang, X. Zhang, W. Shao, Q. Zhang, W. Yan, B. Pan and Y. Xie, *J. Am. Chem. Soc.*, 2018, **140**, 1760–1766.

30 Y. Zhang, J. Zhao, H. Wang, B. Xiao, W. Zhang, X. Zhao, T. Lv, M. Thangamuthu, J. Zhang, Y. Guo, J. Ma, L. Lin, J. Tang, R. Huang and Q. Liu, *Nat. Commun.*, 2022, **13**, 58–67.

31 S. Wang, J. Zhan, K. Chen, A. Ali, L. Zeng, H. Zhao, W. Hu, L. Zhu and X. Xu, *ACS Sustainable Chem. Eng.*, 2020, **8**, 8214–8222.

32 Q. Yang, X. Li, L. Chen, X. Han, F. R. Wang and J. Tang, *Angew. Chem., Int. Ed.*, 2023, **62**, e202307907.

33 G. Li, N. M. Dimitrijevic, L. Chen, T. Rajh and K. A. Gray, *J. Phys. Chem. C*, 2008, **112**, 19040–19044.

34 X. Lang, H. Ji, C. Chen, W. Ma and J. Zhao, *Angew. Chem., Int. Ed.*, 2011, **50**, 3934–3937.

35 H. Liu, C. Xu, D. Li and H. Jiang, *Angew. Chem., Int. Ed.*, 2018, **57**, 5379–5383.

36 G. Kresse and J. Furthmüller, *Comput. Mater. Sci.*, 1996, **6**, 15–50.

37 P. E. Blöchl, *Phys. Rev. B: Condens. Matter Mater. Phys.*, 1994, **50**, 17953–17979.

38 J. P. Perdew, J. A. Chevary, S. H. Vosko, K. A. Jackson, M. R. Pederson, D. J. Singh and C. Fiolhais, *Phys. Rev. B: Condens. Matter Mater. Phys.*, 1992, **46**, 6671–6687.